Dynamics of partial cavitation in an axisymmetric converging-diverging nozzle

Jahangir, Saad; Hogendoorn, Willian; Poelma, Christian

DOI
10.1016/j.ijmultiphaseflow.2018.04.019

Publication date
2018

Document Version
Final published version

Published in
International Journal of Multiphase Flow

Citation (APA)
Jahangir, S., Hogendoorn, W., & Poelma, C. (2018). Dynamics of partial cavitation in an axisymmetric converging-diverging nozzle. *International Journal of Multiphase Flow*, *106*, 34-45. https://doi.org/10.1016/j.ijmultiphaseflow.2018.04.019

International Journal of Multiphase Flow 106 (2018) 34–45

Contents lists available at ScienceDirect

International Journal of Multiphase Flow

journal homepage: www.elsevier.com/locate/ijmulflow

Dynamics of partial cavitation in an axisymmetric converging-diverging nozzle

Saad Jahangir, Willian Hogendoorn, Christian Poelma*

Department of Process & Energy (Faculty 3mE), Delft University of Technology, Leeghwaterstraat 21, 2628 CA, Delft, The Netherlands

ARTICLE INFO

Article history:
Received 8 December 2017
Revised 23 February 2018
Accepted 29 April 2018
Available online 11 May 2018

Keywords:
Partial cavitation
Venturi
Multiphase flow
Re-entrant jet mechanism
Bubbly shock mechanism

ABSTRACT

Partial cavitation dynamics in an axisymmetric converging-diverging nozzle are investigated experimentally. Shadowgraphy is used to visualize and analyze different cavitation regimes. These regimes are generated by changing the global static pressure and flow velocity independently. Cloud cavitation is the most interesting and complex regime, because the shedding of vapor clouds is caused by two different mechanisms: the re-entrant jet mechanism and the bubbly shock mechanism. The dynamics are investigated using a position-time diagram. Using such a diagram we show that for cavitation number $\sigma > 0.95$ the cavity shedding is caused by the re-entrant jet mechanism, and for $\sigma < 0.75$ the mechanism responsible for periodic cavity shedding is the bubbly shock mechanism. Both mechanisms are observed in the transition region, $0.75 < \sigma < 0.95$. The shedding frequencies, expressed as Strouhal numbers, collapse on a single curve when plotted against the cavitation number, except for the transition region. The re-entrant jet mechanism is a pressure gradient driven phenomenon, which is caused by a temporary stagnation point at the cavity front. This leads to stick-slip behavior of the cavity. In the bubbly shock regime, a shock wave is induced by a collapse of the previously shedded vapor bubbles downstream of the venturi, which triggers the initiation of the detachment of the growing cavity. The propagation velocity of the shock wave is quantified both in the liquid and the mixture phase by means of the position-time diagram.

1. Introduction

Cavitation is a phenomenon with mostly negative effects, occurring in a wide variety of applications. For instance, cavitation occurring in turbomachinery may cause erosion of the impeller blades, noise production, and system vibrations, leading to failure fatigue (Balas et al., 2006; Van Terwisga et al., 2009). Intense cavitation occurring at ship propellers is also a problem, because of efficiency drop, wear, and noise production. However, in some cases cavitation can have positive effects, for example, to mix two or more dissimilar fluids such as in marine diesel engines (Avellan, Dupont and Farhat, 1991; Habchi, Gillet, Velghe, Bohbot, Schmid, von Rotz and Herrmann, 2014). Understanding the cavitation physics is important because then the harmful effects of cavitation can be minimized and the positive effects can be maximized.

One interesting form of cavitation is the periodic shedding of cavitation clouds. Due to the complex mix of unsteadiness, two-phase flow dynamics, turbulence and fluid-structure interactions, this is a very complicated research field. In previous research usually three different test geometries are used to visualize this cloud shedding: (1) hydrofoils (Callenaere et al., 2001; Danlos et al., 2014; De Lange and De Bruin, 1997; Foeth et al., 2008; Long et al., 2018), (2) planar converging-diverging nozzles with a rectangular cross-section ("wedges") (Chen et al., 2015; Ganesh et al., 2016; Jana et al., 2016; Croci et al., 2016) and (3) converging-diverging axisymmetric nozzles ("venturis") (Rudolf et al., 2014; Hayashi and Sato, 2014; Tomov et al., 2016; Long et al., 2017). Although in all geometries periodic cloud shedding can be observed, due to the specific shape of each of the geometries, they all have their own characteristic flow dynamics. Generally, the venturi has the highest contraction ratio, due to its shape, which results in a wider dynamic cavitation range. In this research, a venturi has been used, which gives us the ability to clearly distinguish between different cavitation mechanisms due to their more intense nature.

Thus far in the literature, two different mechanisms that initiate periodic cloud shedding are described: the re-entrant jet mechanism and the bubbly shock mechanism. There is also a third mechanism, the side-entrant jet (Foeth et al., 2008; Ji et al., 2013; Peng et al., 2016), which is associated with the part of the re-entrant flow that has a strong spanwise velocity component

* Corresponding author.
E-mail address: c.poelma@tudelft.nl (C. Poelma).

https://doi.org/10.1016/j.ijmultiphaseflow.2018.04.019
0301-9322/

such as in hydrofoils. Decaix and Goncalves (2013) reported on the presence of an oblique mode of the cavity oscillations and Timoshevskiy et al. (2016) concluded that the oblique mode of sheet cavity oscillations associated with the development of the spanwise instability exists for all test objects independent of their shape. Because of the similarity between the side-entrant jet to the re-entrant jet, the side-entrant jet is not discussed in further detail.

In the re-entrant jet mechanism, the occurrence of periodic shedding is generally related to the presence of a re-entrant flow in the closure region of the cavity which forms as the liquid flow outside the cavity reattaches in the closure region (Ganesh, 2015; Bensow, 2011). Knapp (1955) discovered a re-entrant jet by means of high-speed imaging. Different studies towards the velocity of the re-entrant jet have been conducted. Pham et al. (1999) measured the velocity of this jet by means of a surface electrical probe. At different foil positions, the mean velocity of the jet was determined. They found that the velocity of the jet was of an equal order of magnitude to that of the free stream velocity. It was also found that the velocity of the re-entrant jet increased with the distance from the leading edge. They further observed that the frequency of the re-entrant jet, measured with the surface electrical probes, was equal to the cloud shedding frequency, measured by pressure measurements. The authors concluded that the re-entrant jet mechanism drives the cloud cavitation shedding process. Kawanami et al. (1997) also investigated the influence of the re-entrant jet on the cloud shedding. In this study, an obstacle was placed at the wall, in order to prevent the re-entrant jet to proceed to the vapor cloud origin. The re-entrant jet could not proceed and vapor cloud shedding was not observed during this experiment. In this way, they proved that the re-entrant jet is the cause of cavity cloud shedding. Callenaere et al. (2001) stated that two parameters are important for the re-entrant jet: the cavity thickness with respect to the re-entrant jet thickness and the adverse pressure gradient. The latter is the sum of the pressure recovery and the friction losses that the re-entrant jet encounters in order to propagate to the leading edge. If the energy budget provided by the adverse pressure gradient is not sufficient to overcome these friction losses, the re-entrant jet cannot proceed and the unsteady cavitation cloud shedding is not started. This clearly indicates that re-entrant jet cavity shedding is a pressure driven phenomenon. Research towards the shedded cloud velocity was performed by Kubota et al. (1989). They studied the flow structures around unsteady cloud cavitation on a hydrofoil experimentally. To that end, Laser Doppler Anemometry with a conditional sampling technique was used. It was found that the convection velocity of this cloud is lower than the global flow velocity. Stanley et al. (2014) experimentally investigated the re-entrant jet mechanism for periodic cloud shedding in a large-scale cylindrical orifice. They provided a refined mechanism of the re-entrant jet development. Unrestricted optical access to the near-wall region showed the presence of a liquid film throughout the shedding cycle. The mechanism causing the periodic shedding was shown to be a combination of a traveling wave style deformation of the cavity interface and a translational pulse, each with different velocities. Generally, for the re-entrant jet driven cavitating flow a Strouhal number based on the cavity length in the range of 0.18–0.35 is found, irrespective if the flow is external (hydrofoil flow) or internal (venturi flow) (Dular et al., 2012; Ganesh, 2015; Stutz and Reboud, 1997). This Strouhal number (St_l) is defined as:

$$St_l = \frac{fl}{u_0}, \tag{1}$$

where l is the length of the cavity at the time of detachment, the shedding frequency of the cavitation clouds is given by f and u_0 is the free stream velocity of the flow. An alternate definition of the Strouhal number is also used in axisymmetric geometries, in which the throat diameter[1] is used as characteristic length. Therefore, the cavity length (l) is replaced with the throat diameter (d):

$$St_d = \frac{fd}{u_0}. \tag{2}$$

In 1964, the occurrence of condensation shocks in cavitating inducers was predicted by Jakobsen (1964); they were studied experimentally by Reisman et al. (1998) using a hydrofoil. Recently, the bubbly shock mechanism as an initiator of the unsteady cloud cavitation shedding was mentioned by Ganesh (2015). In this study, time-resolved X-ray densitometry was used to visualize the void fraction in the flow field. These experiments were performed on a 2D wedge. Gnanaskandan and Mahesh (2016) performed large-eddy simulations on the same configuration to analyze transitional cavitation behavior. Detailed analysis of velocity and void fraction variations were presented. In Ganesh et al. (2016) the bubbly shock phenomenon is observed. According to the authors, this mechanism starts to play a role when the cavitation number is decreased and by that the void fraction in the cavity is increased. In this situation, the shedding process is initiated by the bubbly shock mechanism instead of the re-entrant jet mechanism. The bubbly shock phenomenon can be explained as follows: at a certain moment, a well-defined void fraction front can be observed in the cavity. This front spans the complete cavity height and propagates upstream in the direction of the wedge apex. If the void fraction front reaches the wedge apex the attached cavity is separated from the wedge apex and the vapor cloud is shed. Wang et al. (2017) reported that a shock wave is generated by the collapse of a large-scale cavity structure, and propagates within the attached cavity. A significant void fraction variation was witnessed across the shock wave front. Based on these observations, it can be argued that cavity shedding in the bubbly shock regime is shock-wave driven.

Arndt et al. (2000) performed an experimental and numerical investigation on a 2D NACA 0015 hydrofoil to understand the two competing mechanisms responsible for the shedding of cloud cavitation. They found that at high values of $\sigma/2\alpha$ (σ is the cavitation number and α is the angle of attack), the re-entrant jet mechanism dominates while at low values of $\sigma/2\alpha$, the bubbly shock mechanism dominates. A sharp transition was observed at $\sigma/2\alpha = 4$.

At the moment, there is limited literature present which quantitatively clearly distinguishes between the re-entrant jet mechanism and the bubbly shock mechanism. We introduce a method based on high-speed visualization and Strouhal numbers to identify and distinguish both mechanisms without the need for void fractions. The data will be used in the future to validate numerical models.

The outline of this paper is as follows: the experimental details are explained in Section 2 of the paper, while Section 3 explains in detail the data processing and methods used to explain the flow dynamics in different cavitation regimes. The results are reported in Section 4. Discussions and the conclusions follow in Section 5 and Section 6, respectively.

2. Experimental details

2.1. Flow facility

In Fig. 1, a picture of the venturi can be seen with its geometrical parameters. This venturi is milled out from a rectangular block of polymethylmethacrylate (PMMA, 'perspex'). The most important property of this material is the high light transmission because the refractive index of perspex is very close to that of water. This

[1] For constant diameter geometries, such as diesel injector nozzles, the characteristic length is simply the diameter.

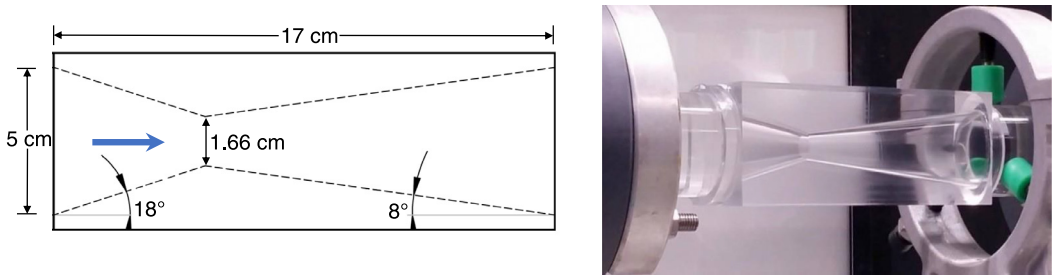

Fig. 1. *(Left)* The geometry and relevant dimensions of the converging-diverging section. *(Right)* Photograph of the venturi in the experimental setup.

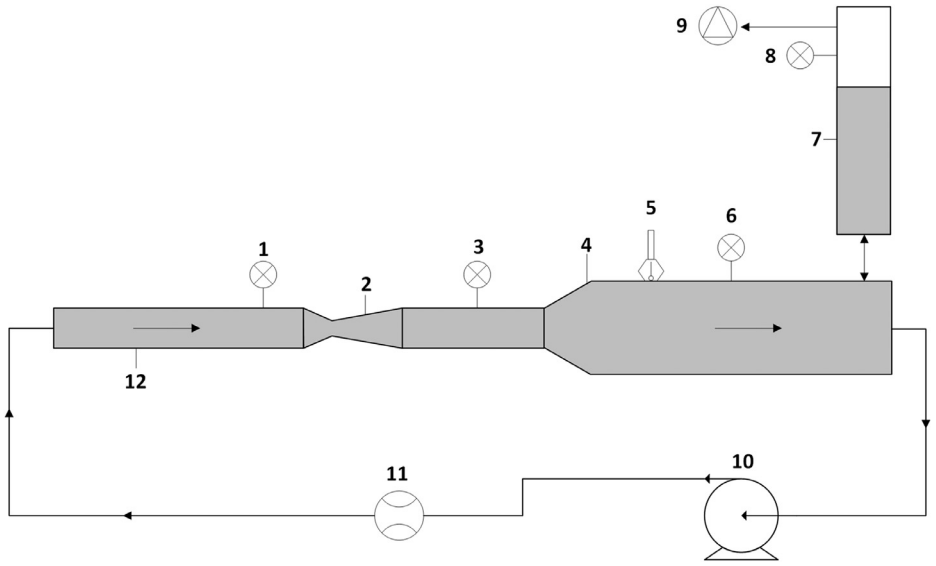

Fig. 2. Schematic overview of the experimental facility. 1,3,6,8-pressure transducers, 2-venturi, 4-pressure recovery section, 5-temperature sensor, 7-water column, 9-vacuum pump, 10-centrifugal pump, 11-electromagnetic flowmeter, 12-inlet pipe.

gives good optical access to the cavitation dynamics. The flow direction is from left to right. The convergence and divergence angles (2α) are 36° and 16° respectively (inspired by previous studies: Rudolf et al., 2014; Long et al., 2017; Tomov et al., 2016; Hayashi and Sato, 2014). The divergence angle of 16° is selected, in order to avoid flow separation while maintaining fairly rapid pressure recovery (Idelchik and Fried, 1986). Furthermore, an area ratio of 1:9 (area of the throat versus exit area) is chosen.

A schematic overview of the experimental setup is given in Fig. 2. The flow in the closed loop system is driven by a centrifugal pump, which is installed 2 m below the measurement section to avoid cavitation in the pump. The volumetric flow rate is measured with a KROHNE flowmeter (type: IFS 4000F/6).

The length available for development is 40D, in order to have a fully-developed turbulent flow entering the test section (Nikuradse, 1932). The upstream pressure transducer is located 0.31 m before the venturi throat and the downstream pressure transducer is located 0.73 m after the venturi throat. The tube after the venturi has a length of 1.4 m. There is a gradual transition from this tube to the pressure recovery section, with an angle of 5.7°, in order to avoid flow separation and minimize flow losses (White, 2003). After this transition, the pressure in the flow is recovered in a pressure recovery section, with an overall length of 1.92 m. Furthermore, temperature measurements are performed in the pressure recovery section.

At the end of the pressure recovery section, a vertical water column is present, to collect the air bubbles entrained in the flow during degasification and to vary the global static pressure of the system. A vacuum pump is used to control the global static pressure below ambient pressure down to 20 kPa absolute.

2.2. Experimental procedure

Before the measurements, the water is degasified using the vacuum pump and a water sample is taken for the determination of the gas content in the system using an oxygen sensor (RDO PRO-X Probe). The setup is operated for a few minutes before the measurement series is started, in order to mix the water in the system to obtain a uniform water temperature. The global static pressure (8 in Fig. 2) of the system is set to a fixed, prescribed value and the measurements are started when the pressure measurements are constant. For the fixed, prescribed global static pressure, measurements are performed at different flow velocities. By means of a data acquisition system, all the sensor values (pressure, flow rate, and temperature) and high-speed images (explained in more detail in the later paragraph) are stored simultaneously. After performing a measurement, the flow velocity is decreased in such a way that cavitation in the venturi is avoided, in order to prevent heating of the system. In the end, the oxygen content is measured again by taking a water sample from the setup. Throughout the paper, the flow conditions will be reported as the cavitation number (σ):

$$\sigma = \frac{p - p_v}{\frac{1}{2}\rho u_0^2}, \tag{3}$$

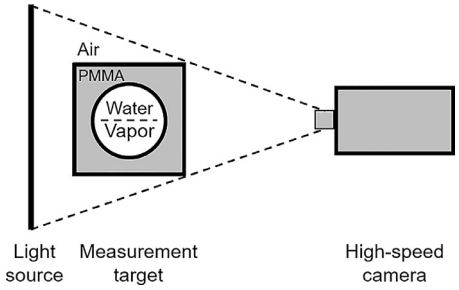

Fig. 3. Sketch of the image capturing technique. The viewing angle in the experiments is smaller than the sketched angle.

where p is the downstream pressure (6 in Fig. 2), p_v is the vapor pressure[2] of the liquid at the temperature of the setup, ρ is the density of the fluid and u_0 is the free stream velocity of the flow at the venturi throat. Furthermore, the pressure loss coefficient K is given by:

$$K = \frac{\Delta p}{\frac{1}{2}\rho u_0^2}, \tag{4}$$

where Δp is the pressure loss over the venturi (calculated from 1 and 3 in Fig. 2).

2.3. Shadowgraphy

The cavity dynamics are captured using shadowgraphy. A schematic overview of this method is shown in Fig. 3. In this method, the measurement target is placed in between a light source and a high-speed camera. The light source illuminates the target from the back side in the direction of the CMOS camera sensor. Preferably a homogeneous light source is used, such as the LED panel used here. Every object that appears in the target blocks the light from the source behind. This results in a dark spot in the camera images. In this way the presence and position of vapor cavities can be determined. As the refractive index of PMMA is relatively close to water the curved inner surface of the venturi did not result in considerable image distortion due to refraction. This was confirmed by placing a calibration target with a regular pattern of markers at the midplane of the venturi. After the calibration an overall uncertainty of less than 1 pixel is found. Please see Hogendoorn (2017) for further explanation.

A high-speed camera (Photron Fastcam APX RS) in combination with a 105mm/2.8 FX AF MICRO-NIKKOR object-glass is used for recording. For the experiments two different acquisition settings are used, in both cases an aperture $f^{\#} = 2.8$ is used as well as a field of view of 1024 × 336 pixels. In the first case, an exposure time of 1/9000 Hz is used in combination with a framerate of 800 Hz and a recording time of 4 s. This video is used for the determination of the cavity shedding frequency. The sample frequency of 800 Hz is selected to meet the Nyquist criterion, because a maximum shedding frequency of 300 Hz is expected.

In the second case a framerate of 9000 Hz is used in combination with an exposure time of 1/9000 Hz and a recording time of 0.1–0.15 s due to practical limitations on the amount of data. This video is used for the cavity length determination and to generate x–t diagrams.

[2] The vapor pressure is calculated using the Antoine equation at the temperature measured during the experiments (14–22.4 °C).

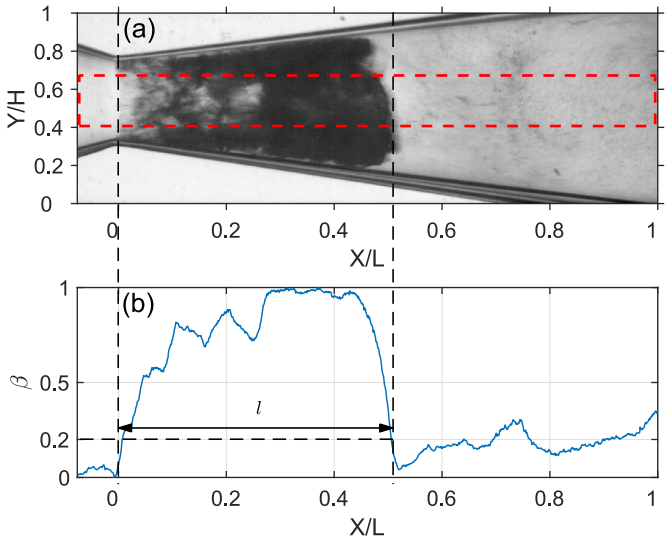

Fig. 4. A typical snapshot showing cavitation in the venturi. The dashed rectangle indicates the region that is used to calculate the average intensity (β). The corresponding result for β as a function of the axial distance is given in the bottom figure, which also shows the method to determine the cavity length. See text for further details on this procedure.

3. Data processing

3.1. Image processing

Fig. 4(a) shows a typical snapshot from a high-speed image sequence. Black indicates the presence of a vapor cavity and the light gray region indicates a liquid phase with some amount of bubbles. It also shows the coordinate system used. As the vertical axis is not used (as will be discussed later), its origin is set arbitrarily. The origin of the horizontal axis, coinciding with the axial/streamwise direction, is set at the throat of the venturi. The axial location (X) is made dimensionless using the length of the diverging section (L). A qualitative comparison of the cavitation dynamics between the horizontal and the vertical plane of the venturi has been performed by placing a mirror at an angle of 45° below the venturi. The side-view and the bottom-view were visualized simultaneously, in order to verify whether the cavitation dynamics are axisymmetric. No significant difference was found, therefore gravity can be neglected. The cavity length at moment of detachment (l) is determined from the average grayscale (β), which can be seen in Fig. 4(b). This average intensity is obtained by averaging the dashed rectangle in Fig. 4a, along the Y-axis. A threshold value of 0.2 is selected to obtain a representative cavity length. The moment of detachment is determined by the gray value at the throat position. When this gray value drops below the threshold value, the cavity is detached. The corresponding length (l) is determined using the preceding frame (i.e. showing the attached state). Since there is a steep gradient in β at the locations of the cavity boundary, the exact details of the threshold method are of minor importance. The lengths determined using this (automated) method also matched visual observations. In order to increase the accuracy of the cavity length determination, an average of five l values is used. An uncertainty analysis points out that the error due to the finite temporal resolution is proportional to $e \propto u_0/F_s$ where F_s is the frame rate, which results in an error of less than 4% of the cavity length.

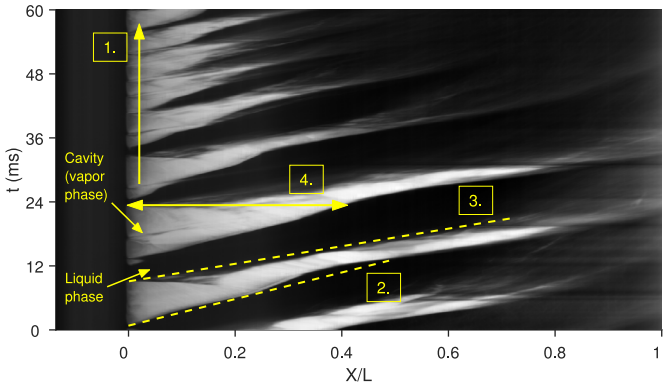

Fig. 5. An x–t diagram, showing the cavitation dynamics. Note that the colors are inverted with respect to the original image (vapor is light gray, liquid is black). The labels are discussed in the text.

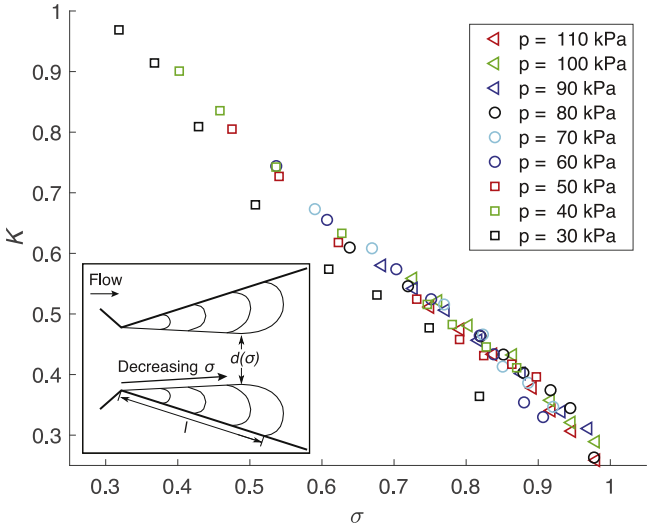

Fig. 6. Pressure loss coefficient (K) as a function of the cavitation number (σ). Only cases with cavitation are shown. The inset shows how the cavitation regions restrict the effective throat area more and more as the cavitation number is lowered.

3.2. X-t diagrams

At each time step, the image data is averaged along the Y-axis over a range spanning $Y/H = 0.4$ to 0.68, corresponding with 100 pixels, as shown in Fig. 4(a). Rectangular averaging is chosen instead of a wedge shape, because variations along the curvature have a small effect. The focus of this research is on global cavitation characteristics, therefore we remove small local variations using this averaging process. This results in a single line of data, representing the instantaneous overall shape of the cavitation cloud. By stacking these lines of data, an x–t diagram is obtained, which will be useful to describe the dynamics of the cavitation process. The x–t diagram is useful for the determination of unsteady cavitation behavior and it is a common data processing method in the field of cavitation (Saito and Sato, 2007; Charrière and Goncalves, 2017; Budich et al., 2018). An example of a typical x–t diagram is shown in Fig. 5. Note that the color-coding is inverted: black represents the liquid phase, while light gray represents the vapor phase.

The frequency of the shedding cycle is determined by performing a Fast Fourier Transform (FFT) in temporal direction (i.e. 'vertical' in an x–t diagram as indicated with arrow 1 in Fig. 5). Different X/L positions can be selected for the FFT. In order to improve the estimate of the frequency, m positions are selected at which the frequency is determined. In the end the frequency is averaged over these m positions. The procedure for $m = 1$ is explained in more detail. A number of signal processing approaches are used for a better frequency determination from this signal. In the first place, this signal is divided into n parts. Subsequently, these parts are multiplied with a hamming window, in order to account for edge effects. From each individual signal the power spectrum is determined by means of an FFT. All n powerspectra are averaged in order to reduce the noise that is present in one spectrum. From this averaged power spectrum the frequency which contains the most power is selected with two neighboring points on both sides. By means of a Gaussian curve fit through these five points, the resolution of the power signal is increased. The frequency corresponding to the maximum point of this Gaussian is determined in order to obtain the final shedding frequency. In case of $m > 1$ positions, the frequencies are averaged along the X dimension as well.

For high shedding frequencies ($\approx$200 Hz) a maximum uncertainty of 5% is found (based on the 95% probability interval), because of the rapid motion. For low shedding frequencies, the dynamics are captured much better, which results in an uncertainty of 1%.

The cavity growth rate and advection velocity are represented by the inverse of the slopes of dashed lines indicated by 2 and 3, respectively. From the shedding frequency and the cavity length at moment of detachment (4), the cavity growth velocity is determined, which is calculated as $u_c = l/t = lf$.

An uncertainty analysis for the shedding frequency determination is performed. To this end, a series with nearly 30,000 shedding cycles is measured and divided into eight parts, where it is assumed that these parts are independent of each other since they contain enough shedding cycles. An uncertainty of less than 5% is found, based on the 95% probability interval. This was also the case for a division of 72 parts, for an entire length of the high-speed image sequence. We conclude that a recording time of 4 s is sufficiently long for frequency determination.

4. Results

4.1. Pressure loss and cavity length

The intensity of cavitation can be described using the cavitation number. With an increase in flow velocity, the cavitation number decreases, suggesting more intense cavitation. For a decreasing cavitation number, we observe that the cavity length increases at the time of detachment. This is schematically visualized for four different cavity lengths in Fig. 6(inset). This figure is an approximation of the cavity behavior observed in the images. It can be seen that the effective throat diameter is narrowed by the presence of the growing cavity, hence the effective throat diameter is a function of σ.

Because of the narrowed throat diameter for decreasing cavitation number, the pressure loss over the venturi will be higher. This is evident from measurement results, shown in Fig. 6. Here the cavitation number is varied by changing the flow velocity at different static pressures, and the pressure loss coefficient K is reported. It can be seen that all points collapse on one line. This implies that flow blockage is a function of cavitation number only (i.e. not of pressure or flow velocity independently). The points corresponding to the global static pressure of 30 kPa are deviating from the global trend because air bubbles are entrained in the circuit due to tiny leakages during the measurements at this relatively low pressure. A linear relation between the pressure loss coefficient and cavitation number was also found by Rudolf et al. (2014).

Fig. 7 schematically shows the pressure and velocity profiles along the throat. The top half shows the velocity profile (solid blue line) based on mass conservation and the bottom half shows the

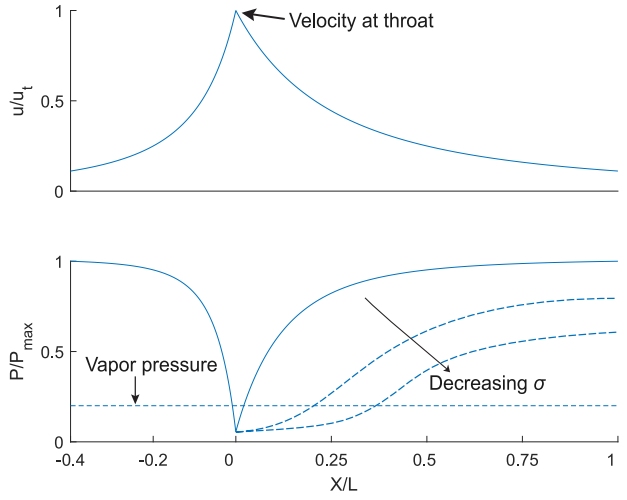

Fig. 7. Schematic representation of the dimensionless velocity and pressure profiles along the throat. The velocity is normalized with the maximum velocity at the throat and pressure with the upstream maximum pressure.

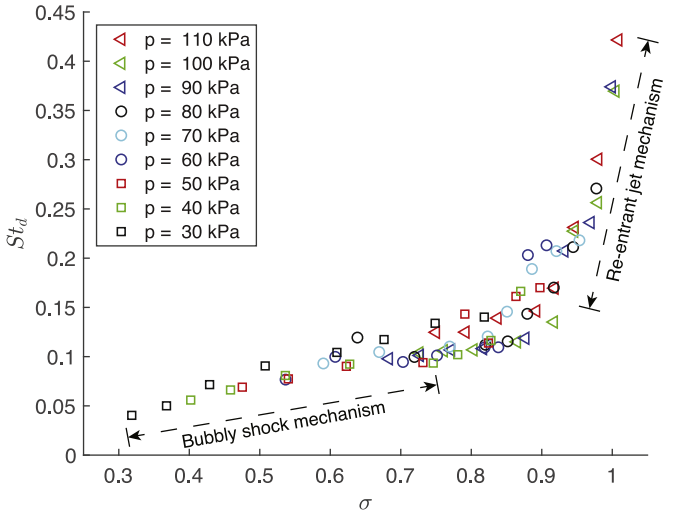

Fig. 9. Dimensionless frequency of the cavitation shedding cycle as a function of the cavitation number.

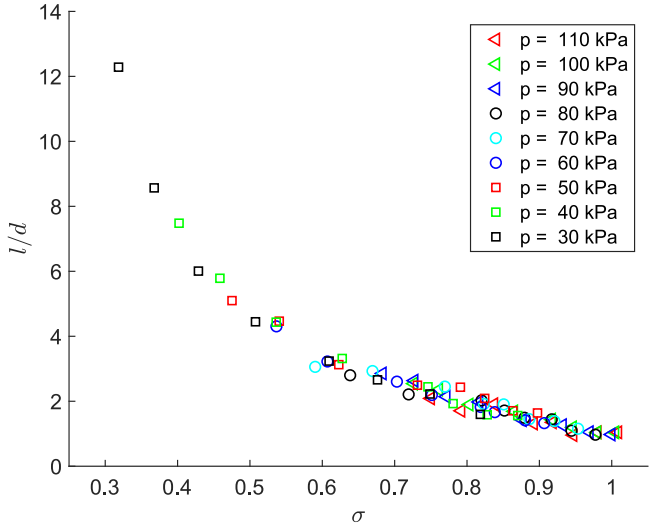

Fig. 8. The average length of the cavity at the time of detachment (scaled with the throat of the venturi) as a function of the cavitation number.

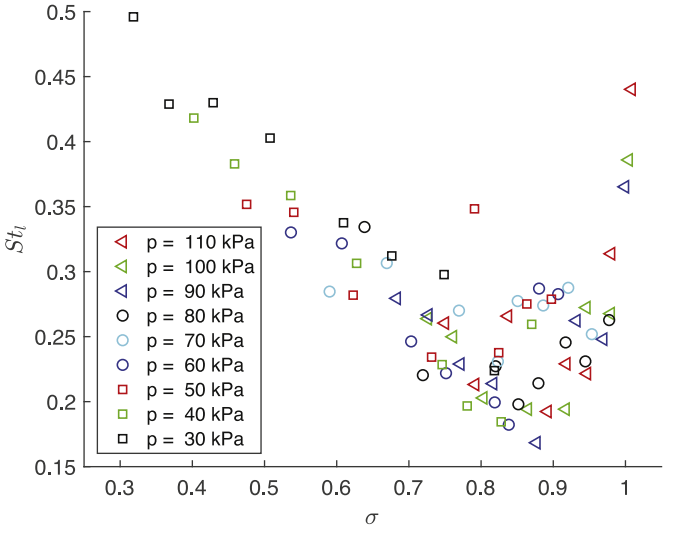

Fig. 10. Cavitation shedding cycle as a function of the cavitation number; the dimensionless frequency is here obtained using the cavity length.

corresponding pressure profile (solid blue line) estimated using the 1D Euler equation. For the cases with a significant cavity, we can no longer predict the pressure using this method. Using the inset of Fig. 6, however, we can predict it qualitatively: for a very low σ we have a very large cavity which extends the effective throat diameter, which leads to a larger high-velocity region. For low σ pressure recovery is thus slower and not complete, as shown by dashed lines (Fig. 7). This is in agreement with the K values reported in Fig. 6. The role of pressure ratio to the cavity length is explained in detail recently by Long et al. (2017). Fig. 7 will be helpful for the interpretation and discussion of the results in Section 5.

The averaged cavity lengths at the time of detachment are also measured as a function of cavitation number and are presented in Fig. 8. The cavity lengths are non-dimensionalized with the throat diameter (d) of the venturi. All measurement points collapse on one curve for the cavitation number based on the global static pressure. For starting cloud cavitation shedding, the dimensionless cavity lengths are of order unity. For decreasing cavitation number, cavities grow longer before detachment, up to 12d in the most extreme case.

4.2. Shedding frequency and temporal development of cavity cloud

The shedding frequency is determined from the x–t diagram as discussed in the previous section. This can be presented in a non-dimensional form with the Strouhal number St_d. The Strouhal number is also a function of cavitation number as can be seen in Fig. 9. It follows that all points collapse on one curve again and the shedding frequency is a function of cavitation number. The inverse of the shedding frequency gives the integral time scale, which corresponds to the process of cavity development to the time of detachment. Multiplication of the shedding frequency with the cavity length scale at the time of detachment gives the global growth rate of the cavity front: $St_l \sim fl/u_0 \sim u_c/u_0$, where u_c is the cavity front velocity. This Strouhal number (St_l) is presented as a function of cavitation number in Fig. 10. It can be seen that not all the points are collapsing on one curve, as in the case of the cavity length and time scales, but nevertheless, a global trend can be observed. A minimum, as well as the highest spread, can be observed for

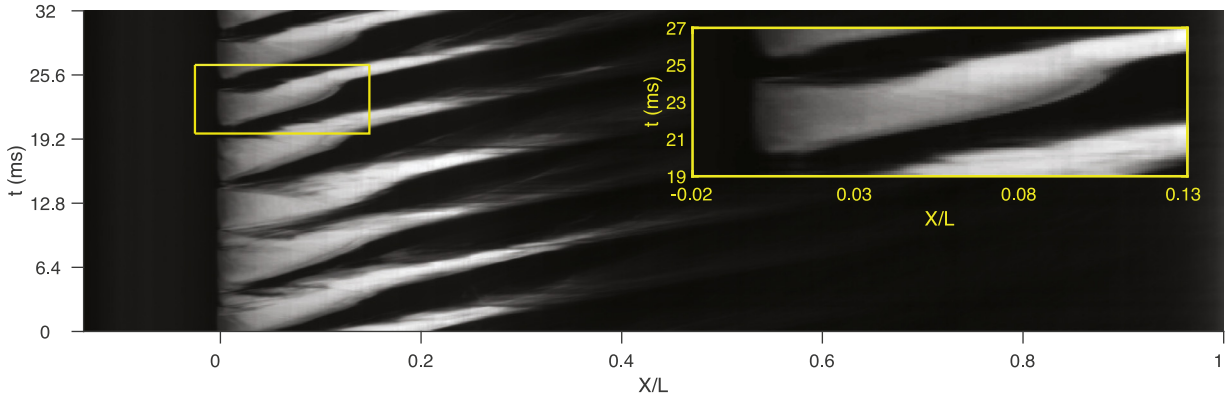

Fig. 11. X–t diagram of an experiment in the re-entrant jet regime. The light gray regions indicate the presence of vapor and the black regions indicate the presence of liquid. An enlargement of a typical shedding cycle is presented in the (yellow) box in the figure. For this case $\sigma = 1$ (corresponding to: $u_0 = 13.5$ m/s, $f = 188.6$ Hz and $p = 90$ kPa). (For interpretation of the references to color in this figure legend, the reader is referred to the web version of this article.)

$0.75 < \sigma < 0.95$. Change is more apparent in frequency/time scales, so we use St_d for further analysis.

From Fig. 9, visual inspection of the video data, and the x–t diagrams (shown and discussed in detail in the next section), two different cavitation mechanisms can be identified as a function of cavitation number. For $\sigma > 0.95$ cloud cavitation shedding is governed by the re-entrant jet mechanism. For $\sigma < 0.75$ cloud cavitation shedding is governed by the bubbly shock mechanism. The cavitation region in between is governed by both mechanisms, so we call it the transition region.[3] For $\sigma < 0.1$, we do not see periodic cavitation: there is strong jet cavitation in this case. The downstream vapor cloud collapse is not strong enough to cause shedding. As the focus of this study is on the dynamics of cavitation, we omit this steady jet cavitation from our analysis.

4.3. Re-entrant jet mechanism and bubbly shock mechanism

From Section 1, it followed that the re-entrant jet mechanism is pressure gradient driven, whereas the bubbly shock mechanism is shock wave driven. To investigate these mechanisms, cavitation characteristics must be examined in more detail. The cavitation essence is well presented in an x–t diagram, because in this diagram the cavity time and length scales are visualized in a clear way. In supplementary data, three movies can be found that further illustrate the findings from the x–t diagrams.

First an x–t diagram for $\sigma > 0.95$ is examined in more detail. From preliminary visual inspection, the re-entrant jet mechanism is expected as a prevalent mechanism for cavity shedding at high σ. To that end the x–t diagram corresponding to a cavitation number of $\sigma = 1$ ($u_0 = 13.5$ m/s, $f = 188.6$ Hz and $p = 90$ kPa) is selected. This diagram is shown in Fig. 11.

The light gray regions indicate the presence of a cavity (vapor) and the black regions indicate the presence of liquid. A typical shedding cycle is captured with a rectangular box and enlarged on the right side of the diagram. It can be seen that this cavity starts to grow at $t \approx 20$ ms and grows linearly until a certain point. After that point the slope becomes steeper, indicating that the cavity front growth rate decreases. During this front velocity decrease, cavity detachment can be observed at $t \approx 24$ ms. The back side of the cavity moves near-instantaneously from $X/L = 0$ to $X/L = 0.04$. This sudden detachment is possibly caused by a pressure gradient. After this sudden detachment, the vapor cloud is advected with a positive velocity. Furthermore, after detachment and partial advection, the cavity front velocity increases to a constant velocity (constant slope). This “stick-slip” behavior is typical for the examined regime. In the stick-slip behavior, the backside (upstream part) of the cavity sticks to the venturi throat and at a certain point this backside suddenly detaches, which is associated with slip. The stick-slip behavior of the re-entrant jet mechanism is also evident in the simulations of Frikha et al. (2008). The re-entrant jet can be observed more clearly by particle/bubble tracking in individual video frames as shown in Fig. 12.

The video frames are chosen for $\sigma = 1$. One complete cycle of the re-entrant jet mechanism and shedding can be seen. The Fig. 12(a) starts at $t/T = 0.11$, where T is the total time of one shedding cycle. It can be seen that the cavitation bubbles start to appear. The re-entrant jet starts to develop (Fig. 12(b)) and this development proceeds to $t/T = 0.56$ (Fig. 12(c)), after which the jet front starts to propagate in the venturi throat direction (Fig. 12(d)). The re-entrant jet front can be recognized by the chaotic interface, which can be seen above the arrow. The propagation of the jet can be seen in Fig. 12(e) and the re-entrant jet reaches the throat and the entire cavity detaches from the throat, as shown in Fig. 12(f). The supplementary movie ‘Movie S1’ shows a few shedding cycles and retrograde motion of the re-entrant jet mechanism. In the movie bubbles/structures can be seen moving upstream, providing further evidence.

From the high-speed images, the mechanism, which causes cavity detachment becomes also clear. In combination with an adverse pressure gradient (the pressure downstream is relatively high and the pressure in the cavity is approximated by the vapor pressure), a re-entrant jet starts to develop. This re-entrant jet disconnects the cavity from the venturi throat, whereafter the cavity is advected with the flow and a new cavity starts to grow.

Re-entrant jet front tracking analysis is performed in order to estimate the re-entrant jet velocity. Typical velocities of 1.1–3.4 m/s are found for mean flow velocities of 14.4–14.8 m/s at the venturi throat (Hogendoorn, 2017).

In Fig. 13, the bubbly shock dynamics are presented in the form of an x–t diagram. A case with a cavitation number of $\sigma = 0.40$ ($u_0 = 13.7$ m/s, $f = 46.1$ Hz and $p = 40$ kPa) is shown. It can be seen that a cavity starts to grow at t $\approx$ 0 ms, with a constant growth rate (linear slope of the black-white interface). At t $\approx$ 12 ms a change in growth rate can be observed (red marker), this is exactly at the point where a nearly horizontal black line (coming from the right) hits the cavity. This black line indicates that there is a liquid phase present in the venturi at this time. It can also be observed that above this black line, at $X/L \approx 0.8$, the previously shed cavity cloud vanishes. It follows that, at the time of cavity collapse,

[3] We see the transition at $\sigma/2\alpha \approx 3$ (where α is the divergence angle) as compared to 4 reported by Arndt et al. (2000). This is likely due to the difference in geometry (venturi versus hydrofoil).

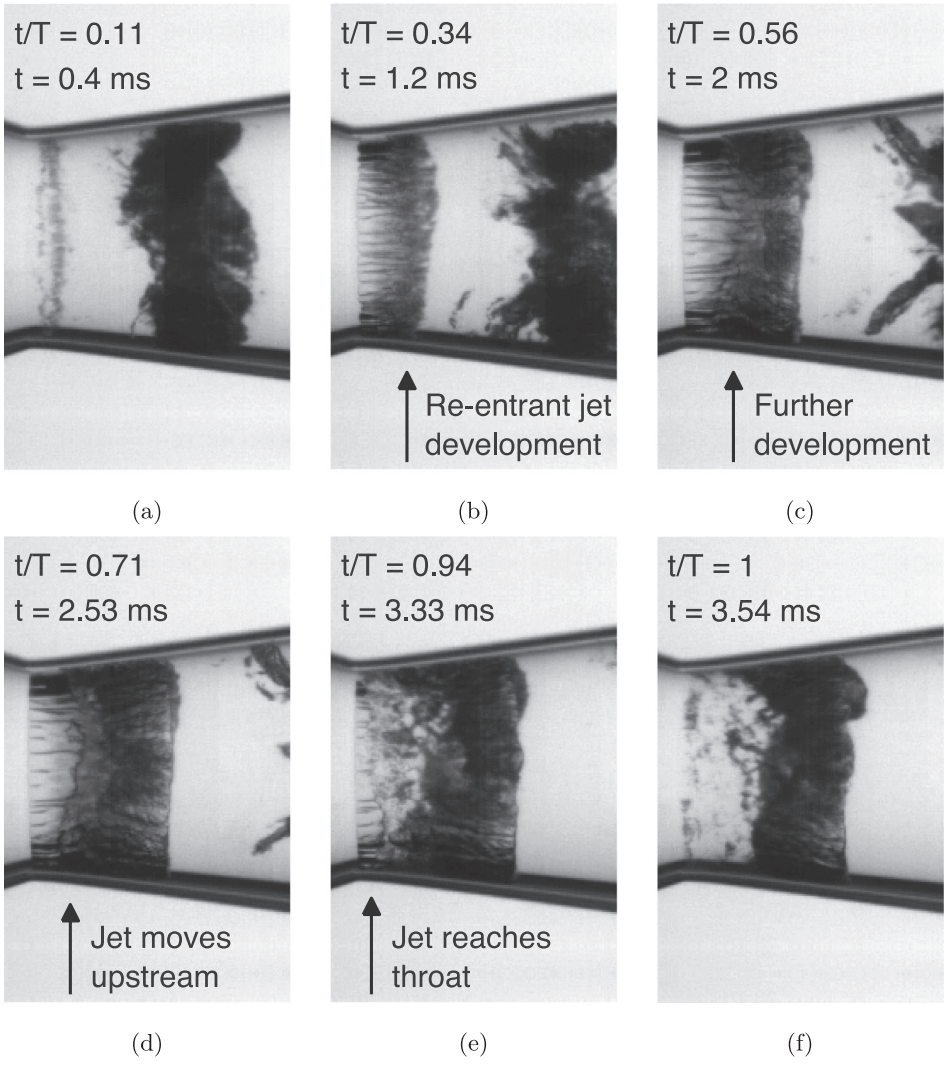

Fig. 12. Video frames of re-entrant jet development at $\sigma = 1$. In Fig. 12(a) and Fig. 12(b), cavity development can be seen. In Fig. 12(c) the re-entrant jet starts to develop. In Fig. 12(d) the jet front can be recognized by the chaotic interface, which can be seen above the arrow. The propagation of the jet front towards the venturi throat can be seen in Fig. 12(e). In the end, cavity detachment is caused by the re-entrant jet as can be observed in Fig. 12(f).

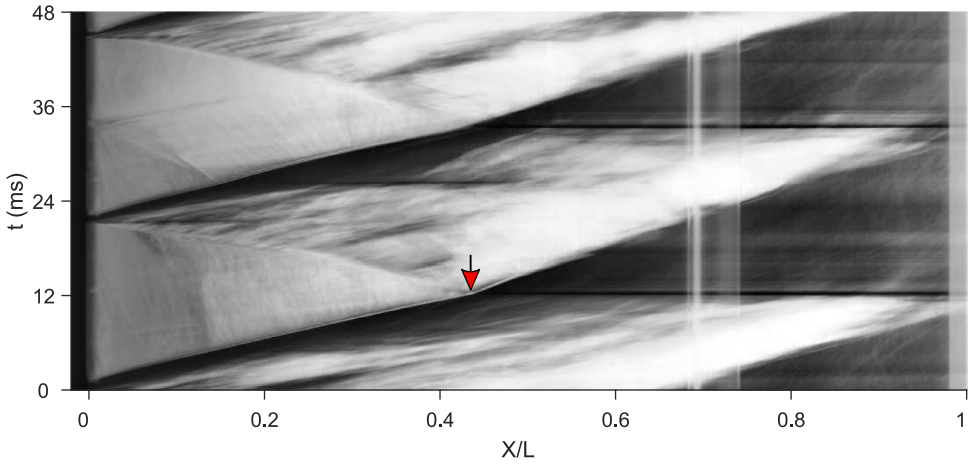

Fig. 13. X-t diagram of an experiment in the bubbly shock regime. The light gray regions indicate the presence of vapor and the black regions indicate the presence of liquid. The cavitation number is $\sigma = 0.40$ ($u_0 = 13.7$ m/s , $f = 46.1$ Hz and $p = 40$ kPa). (For interpretation of the references to color in this figure legend, the reader is referred to the web version of this article.)

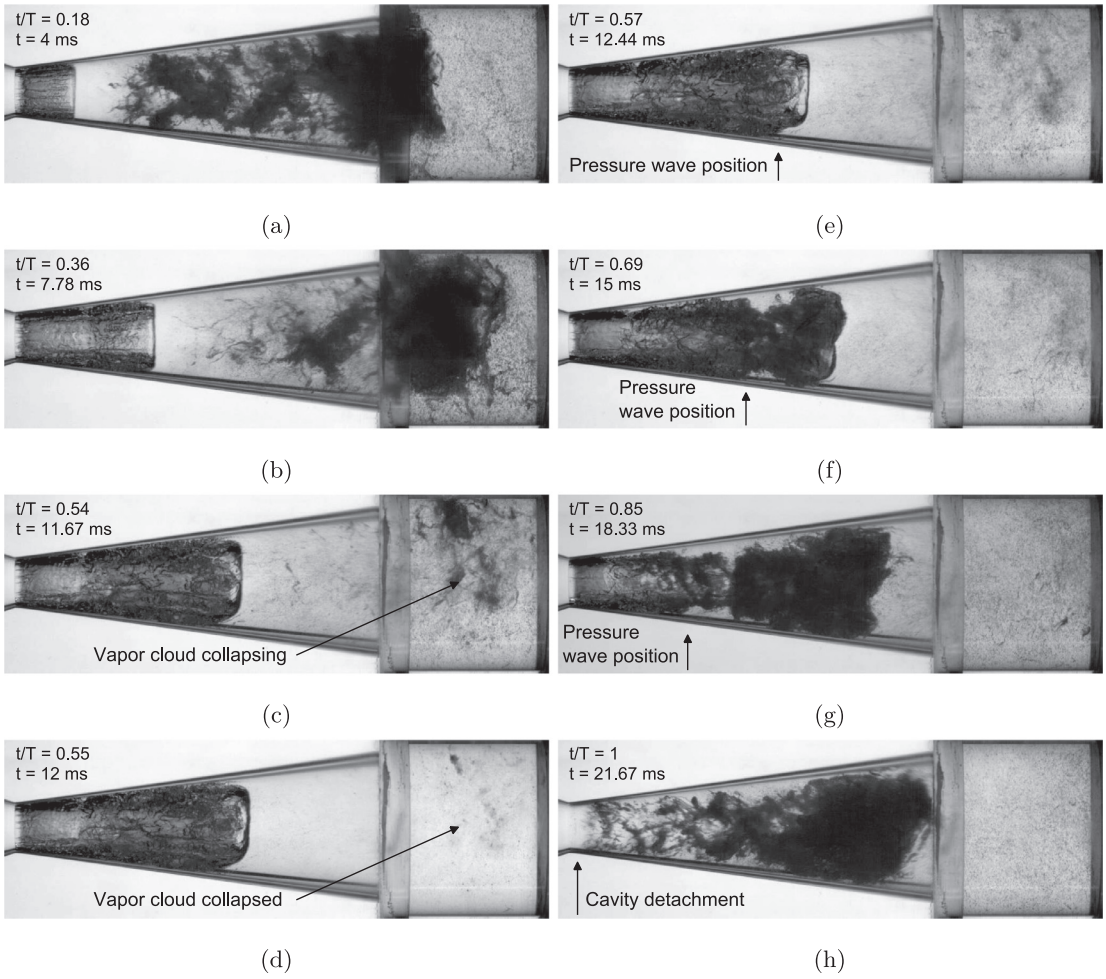

Fig. 14. Video frames of bubbly shock development. In Fig. 14(a) and Fig. 14(b) a growing cavity can be seen (left side of sub-panels) and previously shedded cavity (right side of sub-panels). In the subsequent Fig. 14(c) and Fig. 14(d) the cavity collapses completely and a pressure wave is emitted. The position of this pressure wave is tracked and indicated in Fig. 14(e)–(g). Condensation of the cavity beyond the pressure wave can be seen due to the higher pressure there. Cavity detachment can be observed when the pressure wave reaches the throat (Fig. 14(h)). The cavitation number is $\sigma = 0.40$ ($u_0 = 13.7$ m/s , $f = 46.1$ Hz and $p = 40$ kPa).

a pressure wave is emitted in both directions. The emitted pressure wave is propagating upstream through the growing cavity, as can be seen from the density change in the growing cavity (light gray region). When the pressure wave reaches the venturi throat, the cavity detaches and is thereafter advected with the flow. This shedded cavity also collapses further downstream, again emitting a pressure wave, which is the trigger mechanism for the next cavity detachment.

The corresponding video frames are shown in Fig. 14. Fig. 14(b) and (c) are just before the time of complete cavity collapse. The complete collapse can be seen in Fig. 14(d). The vapor cloud collapses at approximately 10d downstream of the throat. The collapse causes a pressure wave, which is emitted in both directions. In Fig. 14(e)–(g), the position of this (left running) pressure wave is indicated with an arrow. After the passage of the pressure wavefront, a new equilibrium state between the vapor and liquid phase must be formed. Due to the pressure rise after the pressure wavefront, the void fraction in the (growing) cavity decreases by partial condensation. This was also observed in Fig. 13, where a jump in grayscale over the pressure wave was mentioned. When the pressure wave reaches the venturi throat, the cavity detaches, as follows from Fig. 14(h). Wu et al. (2017) also observed a similar pressure wave in a 2D convergent-divergent test section. The supplementary movie 'Movie S2' shows a few shedding cycles for the bubbly shock mechanism.

The velocity of the pressure wave can be calculated from the inverse of the slope in the x–t diagram. First, the pressure wave velocity in the growing cavitation cloud is determined, because this gives important insights about the physics of cavity detachment. The pressure wave path is well described with a second-order polynomial, as can be seen in Fig. 15(a) with a red dashed curve. The velocity of the pressure wave is given by the inverse of the derivative of this path. The pressure wave velocity in the laboratory frame of reference is given by the blue, dashed line in Fig. 15(b). Because the pressure wave travels through the cavity, the absolute velocity of the pressure wave can be best represented by adding the cavity growth rate to the relative pressure wave velocity. This velocity profile is given by the blue, continuous line in Fig. 15(b). It should be remarked that after pressure wave impact (red marker), this cavity growth rate changes, as can be seen from the change in slope, in Fig. 15(a). This change in cavity growth velocity is probably caused by a higher downstream pressure, resulting in a decreasing growth velocity with a factor 1.19 with respect to the growth velocity before impact.

Thus far two typical cases are considered, where either the re-entrant jet mechanism or the bubbly shock mechanism is the prevalent mechanism for cavity shedding. Both mechanisms are observed in the transition region where $0.75 < \sigma < 0.95$. To this end an x–t diagram is shown for an experiment with $\sigma = 0.88$ ($u_0 = 14.2$ m/s, $f = 101.1$ Hz and $p = 90$ kPa), and is presented in

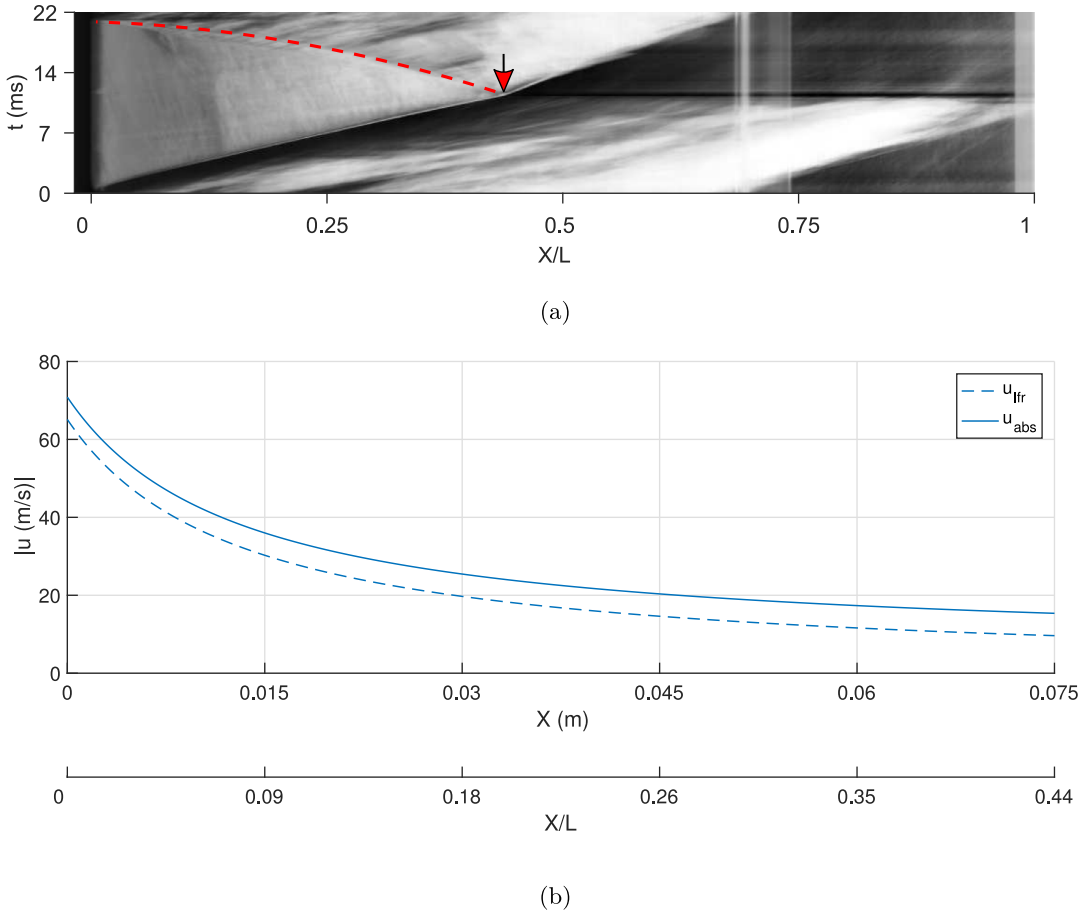

Fig. 15. Pressure wave path with corresponding velocities. In Fig. 15(a) an x–t diagram of the shedding cycle from Fig. 14 is shown. The velocity profiles of the pressure wave as the function of position are shown in Fig. 15(b). The blue dashed line is the velocity in the laboratory frame of reference. The blue continuous line gives the absolute velocity based on the cavity growth rate. Note the difference in horizontal axis scale between the top and bottom figure. (For interpretation of the references to color in this figure legend, the reader is referred to the web version of this article.)

Fig. 16. In this x–t diagram two different regimes can be identified, with a transition at $t \approx 34$ and $t \approx 66$ ms. For $0 < t < 34$ ms and $66 < t < 87.5$ ms emitted pressure waves can be observed, emanating from collapsing cavities. Although the pressure waves are not so evident as in the case of Fig. 13, they can still be identified as the trigger mechanism of (growing) cavity detachment. For $34 < t < 66$ ms, the pattern changes and the characteristics of stick-slip behavior can be observed. This analysis shows that in the intermediate region indeed two alternating mechanisms can be observed. The supplementary movie 'Movie S3' shows a few shedding cycles for the transition region.

5. Discussion

This study has analyzed the mechanisms responsible for partial cavitation in a venturi based on the cavitation number. The cavity lengths and time scales of the re-entrant jet mechanism are smaller than the bubbly shock mechanism, as shown in Fig. 8 and Fig. 9, respectively. The x–t diagram of an intermediate region (Fig. 16) clearly distinguishes between both mechanisms based on the above-mentioned parameters. This implies that there is a critical point when the bubbly shock mechanism takes over the re-entrant jet mechanism. From a close investigation of high-speed movies, we found that the bubbly shock mechanism takes over when a certain minimum amount of vapor cloud collapses downstream of venturi to emit a pressure wave strong enough to detach the growing cavity. Large vapor clouds are formed in the bubbly shock mechanism, because of larger cavity lengths at lower cavitation numbers (see Fig. 7), as a result they emit stronger pressure waves. Several vapor cloud collapses (horizontal black lines) can be seen in a shedding cycle in the bubbly shock mechanism as shown in Fig. 13, the pressure wave emitted from the largest vapor cloud collapse causes the shedding (detachment of the growing cavity). This strong pressure wave causes a jump in the density due to condensation while it propagates through the bubbly water and the cavity, so it can be described as a shock wave. The collapses of individual bubbles and small groups initiate further collapses, and this cascade process results in the shock wave. Smaller vapor cloud collapses are also evident in the re-entrant jet mechanism (Fig. 11) but when the pressure waves are extrapolated upstream of the venturi in the x–t diagrams, it is found that they do not cause the detachment of the growing cavity.

Neither the re-entrant jet mechanism, nor the bubbly shock mechanisms was found to be dominant in the transition region. However, a low-frequency component was found in a spectral analysis (at around 10 Hz). This frequency is caused by switching between both the modes i.e. from the re-entrant jet mechanism to the bubbly shock mechanism and vice versa. This frequency is found to be a function of the static pressure of the system, as it decreases with a decrease in static pressure of the system. In order to ensure that it was not due to the pump, a system frequency analysis was performed. The system was operated for 6 min and it was concluded that no frequency component was captured in the frequency range which was in the region of interest. The de-

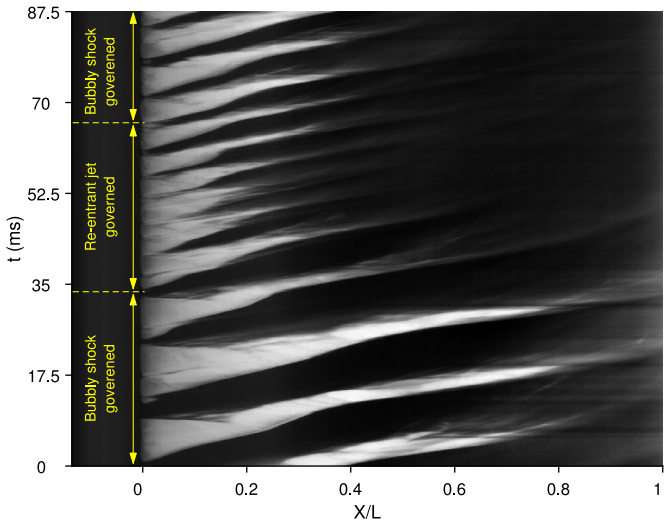

Fig. 16. X-t diagram of an experiment in the intermediate region. The light gray regions indicate the presence of vapor and the black regions indicate the presence of liquid. Bubbly shock induced shedding can be observed for $0 < t < 34$ ms and $66 < t < 87.5$ ms. Re-entrant jet governed shedding can be observed for $34 < t < 66$ ms. For this case, $\sigma = 0.88$ ($u_0 = 14.2$ m/s, $f = 101.1$ Hz and $p = 90$ kPa).

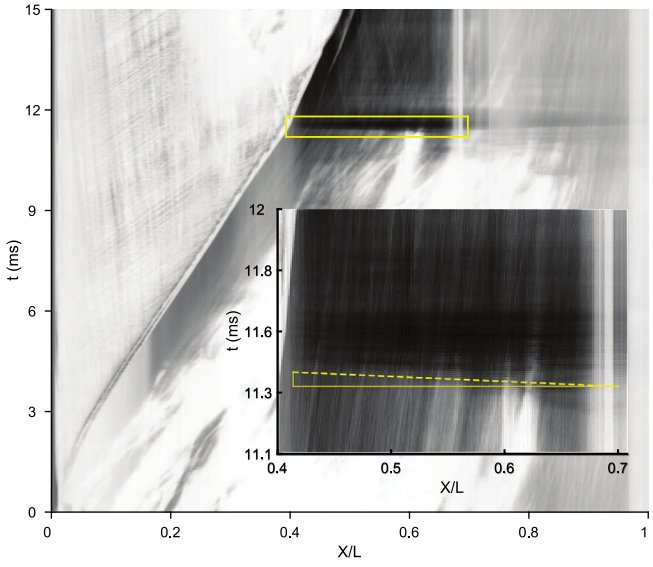

Fig. 17. X-t diagram with an enlarged shock wave path in the liquid phase. The yellow dashed line in the inset gives the best approximation of the shock wave path, corresponding to a velocity of 900 m/s. For this case, $\sigma = 0.40$ ($u_0 = 13.7$ m/s, $f = 46.1$ Hz and $p = 40$ kPa) and $F_s = 125$ kHz. (For interpretation of the references to color in this figure legend, the reader is referred to the web version of this article.)

crease in this frequency causes spreading in the transition region as shown in Figs. 9 and 10.

The dissolved gas concentration can affect the inception of cavitation and mean cavity length, which in turn changes the parameters for the dynamics of cavity deformation. Although the water was degassified before the experiments to approximately 40% oxygen content, still the experiments performed below the ambient pressure at 0.5 bar absolute had an oxygen content of 32% due to unavoidable degassing during experiments.

The shock wave path was tracked through the *cavity*, but there is also a *core* that consists of liquid. Our analysis is based on a single shock wave velocity. The radial variation in vapor fraction will result in different local pressure wave velocities. The speed of sound in the liquid core is of the same order of magnitude as in the liquid region downstream. If the black shock wave path in Fig. 15a is extrapolated through the cavity, a white plume is observed at the throat of venturi ($t \approx 11$ ms). This plume is possibly caused by the shock wave, which traveled through the liquid core region instead of traveling through the cavity.

Accurate determination of the velocity of the shock wave in the liquid region (right side of sub-panels in Fig. 14) was more difficult due to its high velocity. A video was recorded at 125 kHz at $\sigma = 0.4$, the best-approximated shock wave velocity in the liquid phase was found to be 900 m/s by using an x–t diagram (Fig. 17). The shock wave propagation speed is not the expected 1450 m/s in the liquid phase, because it is not a pure liquid (water). Vapor left from the shedded cavity (Fig. 14d) and the presence of non-condensable gas, even a small amount, significantly lowers the speed of sound. A speed of sound of 900 m/s would correspond to a gas fraction of approximately 0.004% (calculated using the model of Minnaert, 1933).

In contrast, a velocity of 15 m/s was found in the cavity region. This decrease in velocity can be explained by the difference in the speed of sound in both phases. With a static pressure of 40 kPa and the estimated velocity, an approximate void fraction of 35% was found at the cavity front. With the increase of velocity in the cavity (Fig. 15(b)) towards the venturi throat, the vapor fraction also increases. The quantitative usefulness of the experiments for the shock wave velocity, including the change in shock wave velocity, should be further evaluated against quantitative void fractions to compare the speed of sound both in the liquid phase and the vapor phase.

6. Conclusions and outlook

The purpose of the current study was to investigate the different cavitation regimes in a converging-diverging axisymmetric nozzle. The different cavitation regimes are generated by systematically changing the global static pressure and flow velocity. From this study, the following conclusions are formulated:

For a cavitation number based on global static pressure, the pressure loss coefficient is found to be a function of cavitation number only. Flow blockage is increasing for decreasing cavitation number. For the same definition of the cavitation number, cavity length and time scales are also a function of cavitation number. Both scales are combined in the Strouhal number, based on the cavity lengths at the time instant of detachment. This St_l is the dimensionless form of the integral cavity growth velocity. It follows that for this Strouhal number, as a function of cavitation number, a minimum is found for a cavitation number $\sigma = 0.88$.

Based on the result, and the cavitation dynamics in the x–t diagrams, three different cloud cavitation shedding regimes can be identified. It is found that for $\sigma > 0.95$, the periodic cavity shedding is caused by the re-entrant jet mechanism. The shedding caused by re-entrant jet mechanism is characterized by stick-slip behavior in the x–t diagram. For $\sigma < 0.75$, the prevalent mechanism for periodic cavity shedding is found to be the bubbly shock mechanism. Both mechanisms are encountered in the intermediate region, $0.75 < \sigma < 0.95$. From a physical point of view, both mechanisms are very different. The re-entrant jet mechanism is caused by an adverse pressure gradient and a stagnation point at the closure of the cavity. The bubbly shock in the growing cavity is caused by a shock wave, which is emitted from the previously detached, advected and collapsing cavity. This makes this mechanism a shock-wave driven phenomenon. The shock wave velocity, as a function of position, is determined from the shock wave path in the x–t diagram. The shock wave velocity in the liquid phase was found to be 900 m/s and around 15 m/s in the cavity region.

The collected data is currently being used for validation of numerical codes. X-ray densitometry experiments are also being per-

formed to extract quantitative information regarding the local void fractions. X-ray experiments will also help us in reconstructing the 3D shape of the cavity.

Acknowledgments

SJ and WH contributed equally to this paper. SJ has received funding from the European Union Horizon 2020 Research and Innovation programme, grant agreement No. 642536. CP and WH have received funding from ERC Consolidator Grant No. 725183 “OpaqueFlows”. We thank S. Schenke (TU Delft) for the many fruitful discussions.

Supplementary material

Supplementary material associated with this article can be found, in the online version, at doi:10.1016/j.ijmultiphaseflow.2018.04.019.

References

Arndt, R.E., Song, C., Kjeldsen, M., He, J., Keller, A., 2000. Instability of partial cavitation: a numerical/experimental approach. In: Proceedings of 23rd Symposium on Naval Hydrodynamics, Val deReuil, France, 17–22 Sept.

Avellan, F., Dupont, P., Farhat, M., 1991. Cavitation erosion power. In: 1st ASME-JSME Fluids Engineering Conference, Portland, OR, 23–27 June.

Balas, G.J., Bokor, J., Vanek, B., Arndt, R.E., 2006. Control of High-Speed Underwater Vehicles. In: Control of Uncertain Systems: Modelling, Approximation, and Design. Springer, pp. 25–44.

Bensow, R.E., 2011. Simulation of the unsteady cavitation on the Delft Twist11 foil using RANS, DES and LES. In: Proceedings of the 2nd International Symposium on Marine Propulsors, Hamburg, Germany.

Budich, B., Schmidt, S., Adams, N., 2018. Numerical simulation and analysis of condensation shocks in cavitating flow. J. Fluid Mech. 838, 759–813.

Callenaere, M., Franc, J.-P., Michel, J.-M., Riondet, M., 2001. The cavitation instability induced by the development of a re-entrant jet. J. Fluid Mech. 444, 223–256.

Charrière, B., Goncalves, E., 2017. Numerical investigation of periodic cavitation shedding in a venturi. Int. J. Heat Fluid Flow 64, 41–54.

Chen, G., Wang, G., Hu, C., Huang, B., Gao, Y., Zhang, M., 2015. Combined experimental and computational investigation of cavitation evolution and excited pressure fluctuation in a convergent-divergent channel. Int. J. Multiphase Flow 72, 133–140.

Croci, K., Tomov, P., Ravelet, F., Danlos, A., Khelladi, S., Robinet, J.-C., 2016. Investigation of two mechanisms governing cloud cavitation shedding: experimental study and numerical highlight. ASME 2016 International Mechanical Engineering Congress & Exposition IMECE 2016.

Danlos, A., Ravelet, F., Coutier-Delgosha, O., Bakir, F., 2014. Cavitation regime detection through proper orthogonal decomposition: dynamics analysis of the sheet cavity on a grooved convergent–divergent nozzle. Int. J. Heat Fluid Flow 47, 9–20.

De Lange, D., De Bruin, G., 1997. Sheet cavitation and cloud cavitation, re-entrant jet and three-dimensionality. Appl. Sci. Res. 58 (1), 91–114.

Decaix, J., Goncalves, E., 2013. Investigation of three-dimensional effects on a cavitating venturi flow. Int. J. Heat Fluid Flow 44, 576–595.

Dular, M., Khlifa, I., Fuzier, S., Maiga, M.A., Coutier-Delgosha, O., 2012. Scale effect on unsteady cloud cavitation. Exp. Fluids 53 (5), 1233–1250.

Foeth, E.-J., van Terwisga, T., van Doorne, C., 2008. On the collapse structure of an attached cavity on a three-dimensional hydrofoil. J. Fluids Eng. 130 (7), 071303.

Frikha, S., Coutier-Delgosha, O., Astolfi, J.A., 2008. Influence of the cavitation model on the simulation of cloud cavitation on 2D foil section. Int. J. Rotating Mach. 2008.

Ganesh, H., 2015. Bubbly Shock Propagation as a Cause of Sheet to Cloud Transition of Partial Cavitation and Stationary Cavitation Bubbles Forming on a Delta Wing Vortex.. The University of Michigan.

Ganesh, H., Mäkiharju, S.A., Ceccio, S.L., 2016. Bubbly shock propagation as a mechanism for sheet-to-cloud transition of partial cavities. J. Fluid Mech. 802, 37–78.

Gnanaskandan, A., Mahesh, K., 2016. Large eddy simulation of the transition from sheet to cloud cavitation over a wedge. Int. J. Multiphase Flow 83, 86–102.

Habchi, C., Gillet, N., Velghe, A., Bohbot, J., Schmid, A., von Rotz, B., Herrmann, K., 2014. On the role of cavitation in marine large diesel injector: numerical investigation of nozzle orifices eccentricity. In: Annual Conference on Liquid Atomization and Spray Systems, Bremen, Germany.

Hayashi, S., Sato, K., 2014. Unsteady behavior of cavitating waterjet in an axisymmetric convergent-Divergent nozzle: high speed observation and image analysis based on frame difference method. J. Flow Control Meas. Visualization 2, 94–104.

Hogendoorn, W., 2017. Cavitation: experimental investigation of cavitation regimes in a coverging-diverging nozzle. Delft University of Technology Master’s thesis. Available online at reposity.tudelft.nl;uuid:823a18f0-66a8-4ffd-a688-c3dadf62c4da

Idelchik, I.E., Fried, E., 1986. Handbook of Hydraulic Resistance: Second Edition, 2nd ed. Hemisphere Publishing, New York, NY.

Jakobsen, J., 1964. On the mechanism of head breakdown in cavitating inducers. J. Basic Eng. 86 (2), 291–305.

Jana, J., Milada, K., Daniel, H., Michal, W., 2016. Methods of experimental investigation of cavitation in a convergent-divergent nozzle of rectangular cross section. Meas. Sci. Rev. 16 (4), 197–204.

Ji, B., Luo, X., Wu, Y., Peng, X., Duan, Y., 2013. Numerical analysis of unsteady cavitating turbulent flow and shedding horse-shoe vortex structure around a twisted hydrofoil. Int. J. Multiphase Flow 51, 33–43.

Kawanami, Y., Kato, H., Yamaguchi, H., Tanimura, M., Tagaya, Y., 1997. Mechanism and control of cloud cavitation. J. Fluids Eng. 119 (4), 788–794.

Knapp, R.T., 1955. Recent investigations of the mechanics of cavitation and cavitation damage. Trans. ASME 77, 1045–1054.

Kubota, A., Kato, H., Yamaguchi, H., Maeda, M., 1989. Unsteady structure measurement of cloud cavitation on a foil section using conditional sampling technique. J. Fluids Eng. 111 (2), 204–210.

Long, X., Cheng, H., Ji, B., Arndt, R.E., Peng, X., 2018. Large eddy simulation and Eulerâ;;Lagrangian coupling investigation of the transient cavitating turbulent flow around a twisted hydrofoil. Int. J. Multiphase Flow 100, 41–56.

Long, X., Zhang, J., Wang, J., Xu, M., Lyu, Q., Ji, B., 2017. Experimental investigation of the global cavitation dynamic behavior in a venturi tube with special emphasis on the cavity length variation. Int. J. Multiphase Flow 89, 290–298.

Minnaert, M., 1933. On musical air-bubbles and the sounds of running water. Lond. Edinburgh Dublin Philos. Mag. J. Science 16 (104), 235–248.

Nikuradse, J., 1932. Gesetzmäβigkeiten der Turbulenten Strömung in Glatten Rohren B, 1. Berlin

Peng, X., Ji, B., Cao, Y., Xu, L., Zhang, G., Luo, X., Long, X., 2016. Combined experimental observation and numerical simulation of the cloud cavitation with U–type flow structures on hydrofoils. Int. J. Multiphase Flow 79, 10–22.

Pham, T., Larrarte, F., Fruman, D., 1999. Investigation of unsteady sheet cavitation and cloud cavitation mechanisms. J. Fluids Eng. 121 (2), 289–296.

Reisman, G., Wang, Y.-C., Brennen, C.E., 1998. Observations of shock waves in cloud cavitation. J. Fluid Mech. 355, 255–283.

Rudolf, P., Hudec, M., Gríger, M., Štefan, D., 2014. Characterization of the cavitating flow in converging-diverging nozzle based on experimental investigations. In: EPJ Web of Conferences, 67. EDP Sciences.

Saito, Y., Sato, K., 2007. Bubble collapse propagation and pressure wave at periodic cloud cavitation. In: Proceedings of 6th International Conference on Multiphase Flow, ICMF 2007.

Stanley, C., Barber, T., Rosengarten, G., 2014. Re-entrant jet mechanism for periodic cavitation shedding in a cylindrical orifice. Int. J. Heat Fluid Flow 50, 169–176.

Stutz, B., Reboud, J., 1997. Experiments on unsteady cavitation. Exp. Fluids 22 (3), 191–198.

Timoshevskiy, M.V., Churkin, S.A., Kravtsova, A.Y., Pervunin, K.S., Markovich, D.M., Hanjalić, K., 2016. Cavitating flow around a scaled-down model of guide vanes of a high-pressure turbine. Int. J. Multiphase Flow 78, 75–87.

Tomov, P., Khelladi, S., Ravelet, F., Sarraf, C., Bakir, F., Vertenoeuil, P., 2016. Experimental study of aerated cavitation in a horizontal venturi nozzle. Exp. Therm. Fluid Sci. 70, 85–95.

Van Terwisga, T., Li, Z.-r., Fitzsimmons, P., Foeth, E.J., 2009. Cavitation erosion - a review of physical mechanisms and erosion risk models. Proc. 7th Int. Sym. Cavitation, CAV2009, Ann Arbor, MI.

Wang, C., Huang, B., Wang, G., Zhang, M., Ding, N., 2017. Unsteady pressure fluctuation characteristics in the process of breakup and shedding of sheet/cloud cavitation. Int. J. Heat Mass Transf. 114, 769–785.

White, F.M., 2003. Fluid Mechanics, 7th ed. McGraw-hill.

Wu, X., Maheux, E., Chahine, G.L., 2017. An experimental study of sheet to cloud cavitation. Exp. Therm Fluid Sci. 83, 129–140.